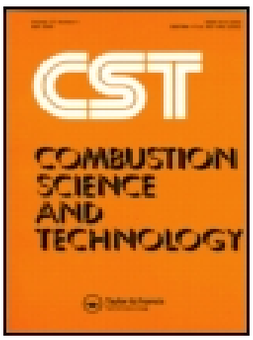

Taylor & Francis
Taylor & Francis Group

Combustion Science and Technology

ISSN: 0010-2202 (Print) 1563-521X (Online) Journal homepage: http://www.tandfonline.com/loi/gcst20

Extinction Analysis of a Methane-Oxygen Counterflow Flame at High Pressure

Albert Jordà Juanós & William A. Sirignano

To cite this article: Albert Jordà Juanós & William A. Sirignano (2017): Extinction Analysis of a Methane-Oxygen Counterflow Flame at High Pressure, Combustion Science and Technology, DOI: 10.1080/00102202.2017.1367293

To link to this article: http://dx.doi.org/10.1080/00102202.2017.1367293

Accepted author version posted online: 21 Aug 2017.
Published online: 21 Aug 2017.

COMBUSTION SCIENCE AND TECHNOLOGY
https://doi.org/10.1080/00102202.2017.1367293

Taylor & Francis
Taylor & Francis Group

Extinction Analysis of a Methane-Oxygen Counterflow Flame at High Pressure

Albert Jordà Juanós and William A. Sirignano

Department of Mechanical and Aerospace Engineering, University of California Irvine, CA, USA

ABSTRACT

A numerical study on a high-pressure laminar counterflow diffusion flame is presented. Extinction limits are studied at pressures up to 100 atm for two cases: one with pure methane and the other for a diluted mixture of methane with 40% water vapor mass fraction. The fuel stream flows against pure oxygen on both cases. Solutions for the 1D ideal-gas model and for a real-gas model are provided with both detailed and reduced chemical kinetics, and are compared against real-gas results from the literature. Previous studies increased the strain rate by rising the inflowing velocities of the opposing streams, yielding very high speeds near extinction. Here, strain rate is increased mainly by moving the nozzles closer to each other and also by small increases in the inflow velocities until extinction occurs. When no water is present, there is good agreement in the extinction strain rate between all the cases. However, substantial differences appear in extinction temperature, which features a local minimum between 70 atm and 90 atm, which was not previously reported in the literature. Furthermore, when water vapor is mixed with the fuel, both extinction strain rate and extinction temperature behave differently with increasing pressure. Extinction strain rate increases with pressure and reaches an asymptotic value at about 50 atm, while extinction flame temperature increases from 1 atm to 20 atm, and then decreases almost linearly.

ARTICLE HISTORY
Received 3 March 2017
Revised 9 August 2017
Accepted 10 August 2017

KEYWORDS
Extinction; Counterflow; High pressure; Methane; Reduced kinetics

Introduction

Combustion of hydrocarbons at high pressures is important in applications such as liquid-rocket, gas-turbine, or diesel engines. Current efforts pursue higher efficiencies and lower emissions of pollutants. The counterflow canonical configuration has been extensively used to study both premixed and diffusion flames (Law, 2006; Williams, 1985). Even though turbulent counterflow-flame investigations are becoming more common (Coppola et al., 2009; Kempf et al., 2000; Kim and Mastorakos, 2006; Pettit et al., 2011; Tirunagari and Pope, 2017), literature on laminar-flame analyses is still predominant. The goal is to provide conclusions that apply to more realistic turbulent situations, where laminar-flamelet solutions apply locally (Marble and Broadwell, 1977).

A broad range of experimental studies exists, but most of them are at atmospheric pressure (Ricchiuti et al., 2013; Sung et al., 1995). High-pressure experimental results have been published up to 25 atm (Figura et al., 2015; Niemann et al., 2014; Piller et al., 2015)

CONTACT Albert Jordà Juanós ajordaju@uci.edu Department of Mechanical and Aerospace Engineering, University of California Irvine, 4200 Engineering Gateway, Irvine, CA 92697-3975, USA.

Color versions of one or more of the figures in the article can be found online at www.tandfoline.com/gcst.

and there are research groups pursuing higher pressure values that compare to the nominal magnitudes in the applications such as those mentioned above (i.e., $p > 60$ atm). At these high-density values, real-gas effects become important. In light of this, numerical studies entailing real-gas models have recently received more attention (Huo et al., 2014; Ribert et al., 2008; Wang et al., 2015). Whereas some previous publications used ideal-gas models, these more recent and sophisticated analyses for real gases did not provide error estimates on the typical approximations.

In a previous study on methane-air counterflow diffusion flame at high pressure, Jordà Juanós and Sirignano (2017) provided comprehensive results comparing ideal with real-gas solutions, and also with cases entailing a combination of a real-gas model with certain ideal-gas approximations. The pressure range was between 1 atm and 100 atm. The goal was to isolate each of the approximations that are commonly taken (i.e., the use of the ideal-gas law, perfect-gas relationships in the energy equation, and ideal-gas transport properties). A path for error estimates was identified in the counterflow canonical configuration such that it could serve as a template for other researchers. The conclusion was that the largest source of error is the use of the ideal-gas law rather than a more accurate cubic equation of state, followed by the use of a simplified energy equation, while use of ideal-gas transport properties is less significant. Substantial differences appeared mainly in terms of flame location. The use of a simplified version of the energy equation resulted in higher flame temperatures. They also introduced the use of the mixture enthalpy computed from the mixing rules associated to the cubic equation of state, as opposed to the approximation that the mixture enthalpy equals the summation of the partial enthalpies times the mass fractions of the species. This approximation is commonly taken even in studies that claim to use a full real-gas model. The associated error was shown to be below 3%. Turbulence generation, radiative heat losses, and the Soret effect were demonstrated to be essentially negligible under certain attainable conditions, even at the highest pressure. Chemical equilibrium results with the use of fugacities were compared with results using partial pressures. Differences of at most 1% indicate that current chemical kinetic laws may predict equilibrium and rates accurately, even though chemical pathways may still be different at high pressures.

The most complete real-gas model was also applied to report solutions where water vapor was premixed with the methane stream. It was concluded that presence of water not being generated as a combustion product acts as an energy sink, therefore flame temperatures decrease with increasing water content. Escalation of pressure produced similar effects on the flame for both the cases with inflowing water and without it. These effects include increase of flame temperature, narrowing the flame region, and displacement of the flame position closer to the stagnation plane.

With the given context, our previous analysis is extended in the present study for a methane-oxygen diffusion flame. Here, the most complete model, presented in the second and third sections, is used to analyze three important aspects: (i) comparison between the use of detailed kinetics and reduced kinetics; (ii) flame extinction analysis where the fuel is pure methane and where it is a mixture of methane and 40% water vapor. Comparisons are made among real-gas model with detailed kinetics, real-gas model with reduced kinetics, real-gas results from the literature, and ideal-gas model; and (iii) effect of varying the mass-flow-rate ratio of the two counterflow streams. Results are presented in the fourth section, with a summary of conclusions given in the last section.

Model

Figure 1 shows a sketch that represents the axisymmetric flow between two circular opposed jets and the flame that is generated. Pure methane flows from the top nozzle while oxygen flows from the bottom. Under the boundary-layer approximation, the 2D problem may be simplified to a system of ordinary differential equations (ODEs) with the independent variable that is the x-coordinate normal to the stagnation plane (Kee et al., 1988; Smooke et al., 1986). Slightly different formulations are available, depending on which parameter is chosen to alter the strain. Prescribing the momentum fluxes at the exit of the nozzles fixes the radial pressure gradient and the strain rate of the problem, or vice versa. The approach described by Kee et al. (1988) is followed with modifications in the energy equation and the equation of state.

The governing equations are summarized below, starting with the steady-state continuity equation in cylindrical coordinates.

$$\frac{\partial(r\rho u)}{\partial x}+\frac{\partial(r\rho v)}{\partial r}=0 \tag{1}$$

The stream function is introduced as $\Psi(x,r)\equiv r^2F(x)$, which satisfies the steady-state continuity equation exactly if

$$\frac{\partial\Psi}{\partial r}=r\rho u=2rF \quad \text{and} \quad -\frac{\partial\Psi}{\partial x}=r\rho v=-r^2\frac{dF}{dx} \tag{2}$$

Then, the axial velocity u depends only on x and the radial velocity v varies linearly in r. The temperature T and species mass fractions Y_k are also functions of x only. Using the small Mach number approximation, the thermodynamic pressure p is assumed to be constant in the equation of state but pressure-gradient terms are allowed in the momentum equations, where the term $d(r\tau_{rr})/dr$ associated with the stress in the radial direction is neglected from the boundary-layer analysis. With these considerations and neglect of body forces, the momentum equations reduce to third-order ordinary differential equations. From these equations, an eigenvalue independent of x appears: $H=r^{-1}dp/dr$.

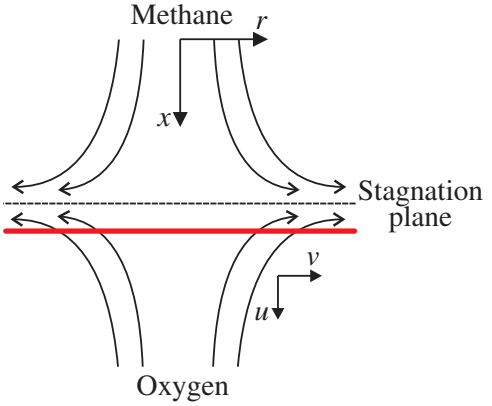

Figure 1. Non-premixed counterflow axisymmetric configuration.

Define the function $G(x) = dF/dx$. Then, the radial momentum equation becomes a second-order ODE rather than one of third order:

$$H - 2\frac{d}{dx}\left(\frac{FG}{\rho}\right) + \frac{3}{\rho}G^2 + \frac{d}{dx}\left[\mu\frac{d}{dx}\left(\frac{G}{\rho}\right)\right] = 0 \tag{3}$$

where μ is the viscosity.

The species continuity equation is:

$$2F\frac{dY_k}{dx} + \frac{d}{dx}(\rho Y_k V_k) - W_k\dot{\omega}_k = 0 \quad k = 1, 2, ..., K \tag{4}$$

where the index k identifies each species and K is the total number of species.

The energy equation for real gases is:

$$2F\left(\frac{dh}{dx} - \sum_{k=1}^{K} h_k\frac{dY_k}{dx}\right) - \frac{d}{dx}\left(\lambda\frac{dT}{dx}\right) + \rho\sum_{k=1}^{K} Y_k V_k\frac{dh_k}{dx} + \sum_{k=1}^{K} W_k h_k\dot{\omega}_k = 0 \tag{5}$$

where h_k is the specific enthalpy, W_k are the species molecular weights, and $\dot{\omega}_k$ is the rate of consumption. The detailed reaction mechanism GRI 3.0 (Smith et al., 2000) is selected, which consists of $K = 53$ species and 325 elementary reactions. h_k is computed from fundamental thermodynamic theories as the summation of the ideal-gas enthalpy plus a departure function that accounts for dense fluid effects (see the next section). It includes both the heat of formation and the sensible enthalpy. Heat losses due to radiation are neglected. The viscosity μ and thermal conductivity λ are evaluated with empirically correlated functions that were developed to extend kinetic-gas theory to include dense fluids (Chung et al., 1988).

V_k is the diffusion velocity and it is evaluated using the multicomponent formulation (Turns, 2011), in which both pressure and Soret effects have been neglected:

$$V_k = \frac{1}{X_k\overline{W}}\sum_{j=k}^{K}\mathcal{D}_{kj}W_k\frac{dX_k}{dx} \tag{6}$$

X_k are the species mole fractions, $\overline{W}$ is the mean molecular weight, and $\mathcal{D}_{kj}$ are the ordinary multicomponent diffusion coefficients. Ideal-gas thermodynamic and transport properties, as well as the reaction rates, are obtained from the CHEMKIN (Reaction Design, 2013) library of subroutines.

The eigenvalue $H = constant$, the function $G = dF/dx$, Eqs. (3)–(5), together with the equation of state (see the next section), form a well-posed boundary-value problem, where the unknowns are H, F, G, Y_k, T, and ρ. For the given chemical mechanism involving K species, the total number of differential equations is $K + 3$ and the number of difference equations is $N(K + 3)$, where N is the number of grid points. L is the distance between the two nozzles. The solution method is discussed by Jordà Juanós and Sirignano (2017). Plug-flow boundary conditions are specified at the exit of the nozzles. As described by Niemann et al. (2015), these conditions can be reproduced accurately in laboratory experiments. In the following, F and O stand for fuel and oxidizer, respectively.

At $x = 0$:

$$F = \frac{\rho_F u_F}{2} \qquad G = 0 \qquad T = T_F \qquad Y_k = (Y_k)_F \tag{7}$$

At $x = L$:

$$F = \frac{\rho_O u_O}{2} = -\frac{\rho_F u_F}{2} \qquad G = 0 \qquad T = T_O \qquad Y_k = (Y_k)_O \tag{8}$$

The velocities at the exit of the nozzles are prescribed using the equations below. These are useful to analyze the variation of mass-flow rate ratio between the two nozzles at constant strain rate, and also the opposite case, where strain rate is varied and the mass-flow rate ratio is constant. We express the inflow velocities as a function of strain rate and mass-flow rate ratio. Given that for stoichiometric conditions with oxygen and methane $(\dot{m}_O/\dot{m}_F)_s = 4$, we define the oxygen-to-fuel mass-flow rate equivalence ratio as:

$$\Phi = \frac{(\dot{m}_O/\dot{m}_F)}{(\dot{m}_O/\dot{m}_F)_s} = 4\left(\frac{\rho_O}{\rho_F}\right)\left(\frac{u_O}{u_F}\right) \tag{9}$$

where the subscript s denotes stoichiometric ratio. The density ratio will be prescribed for any case in which pressure, temperature, and mass fractions are prescribed at the boundaries.

Define the global strain rate as:

$$s_r = \frac{(u_F - u_O)}{L} = \frac{\hat{s}_r}{L} \tag{10}$$

If we prescribe both Φ and $\hat{s}_r$, then u_F and u_O are determined:

$$u_O = \frac{-1}{1 + \frac{1}{4\Phi}\left(\frac{\rho_F}{\rho_O}\right)} \qquad u_F = \hat{s}_r + u_O \tag{11}$$

Equation of state

The Soave–Redlich–Kwong Equation of State (EoS) is selected because of its reasonable accuracy for a wide range of fluid states (Soave, 1972):

$$p = \frac{R_u T}{v - b} - \frac{a}{v(v + b)} \tag{12}$$

This empirical equation, which may be rearranged to a cubic form with regards to the molar volume v, has two parameters a and b, which are constants for single-component fluids, but become composition, pressure, and temperature dependent in the multicomponent version. The cubic form in terms of the compressibility factor Z is:

$$Z^3 - Z^2 + (A - B - B^2)Z - AB = 0 \tag{13}$$

where

$$Z \equiv \frac{pv}{R_u T} \qquad A \equiv \frac{ap}{(R_u T)^2} \qquad B \equiv \frac{bp}{R_u T} \tag{14}$$

The parameter mixing rules of the Soave–Redlich–Kwong EoS are employed (Soave et al., 2010):

$$a = \sum_{i=1}^{K} \sum_{j=1}^{K} X_i X_j (a_i a_j)^{0.5} (1 - k_{ij}) \qquad b = \sum_{i=1}^{K} X_i b_i \tag{15}$$

The pure species attractive and repulsive parameters a_i and b_i may be obtained from the species critical points as:

$$\begin{aligned} a_i &= a_{ci}\alpha_i \qquad a_{ci} = 0.42748 \frac{(R_u T_{ci})^2}{P_{ci}} \qquad \alpha_i^{0.5} = 1 + S_i(1 - T_{ri}^{0.5}) \\ S_i &= 0.48508 + 1.5517\omega_i - 0.15613\omega_i^2 \qquad b_i = 0.08664 \frac{R_u T_{ci}}{P_{ci}} \end{aligned} \tag{16}$$

where T_{ci} and P_{ci} are the critical temperature and critical pressure of mixture component i, k_{ij} is the characteristic binary interaction constant, and ω_i are the acentric factors. These values are taken from the literature (Prausnitz et al., 1999). Sub-index r stands for "reduced" and equals the property temperature or pressure divided by its critical value. All the attractive and repulsive parameters of chemically stable species such as H_2, O_2, N_2, H_2O, or metastable species like H_2O_2, may be determined from critical states conditions. However, chemically unstable species such as radicals do not have associated critical states, thus not allowing straightforward calculation of their attractive and repulsive terms. Assuming that the ith species is a Lennard–Jones gas, for instance, it is possible to estimate the critical volume $v_{c,i}$ and the critical temperature $T_{c,i}$ (Giovangigli et al., 2011) and to obtain that:

$$a_i = (5.55 \pm 0.12) n \in_i \sigma_i^3 \qquad b_i = (0.855 \pm 0.018) n \sigma_i^3 \tag{17}$$

where n is the Avogadro number, σ_i and $\in_i$ are the molecular diameter and Lennard–Jones potential well depth of the ith species, respectively.

The specific enthalpy departure function is given by:

$$h - h^* = \frac{1}{\overline{W}} \left\{ R_u T(Z-1) + \int_{\infty}^{v} \left[T \left(\frac{dP}{dT} \right)_v - P \right] dv \right\} \tag{18}$$

where h^* is the enthalpy for an ideal gas at the given temperature and with the same composition. This departure function can be determined using the EoS (Rao, 1997):

$$h - h^* = \frac{1}{\overline{W}} \left[R_u T(Z-1) + \frac{T\frac{da}{dT} - a}{b} \ln \frac{Z+B}{Z} \right] \tag{19}$$

Results and discussion

The results are organized in three subsections. First, solutions obtained using detailed kinetics (GRI 3.0) are compared to results using reduced kinetics. Extinction properties are studied in the next subsection, where strain rate is increased while keeping a constant stoichiometric mass-flow rate ratio $\Phi = 1$. Finally, the mass-flow-rate ratio variation at constant strain rate is presented. Pressure ranges between 1 atm and 100 atm.

Reduced kinetics

The goal of this subsection is to compare the results obtained using detailed kinetics (GRI 3.0) with those obtained using reduced kinetics. A 19-species and 15-step reduced mechanism for methane and oxygen is selected (Lu and Law, 2008).

First, at a low strain rate that is far from extinction, results obtained using both detailed and reduced kinetics are compared for different pressures. See in Figure 2a that the curves are almost perfectly superimposed.

At high strain rate, the differences are still small but more noticeable. Figures 2b and 2c show the velocity and temperature when $p = 100$ atm, $\Phi = 1$, and the strain rate is the maximum possible before extinction occurs. We can see in Figure 2b that the local velocity peaks are slightly higher for the reduced kinetics case. This is caused by the greater flame temperature that is also obtained with reduced kinetics, as shown in Figure 2c. The difference in peak temperature is 37.3 K (1.22%) and the difference in flame location is 18.5 nano meters, which represents a 0.2% of L for this case.

Extinction

Flame extinction is examined in this subsection. Extinction occurs when the flow time scale becomes sufficiently lower than the chemical time scale. The inverse of the global strain rate is a good measure of the characteristic time scale. Thus, the counterflow diffusion flame extinguishes when the strain rate is increased until it reaches a certain value known as the extinction strain rate. Previous studies by Ribert et al. (2008), Huo

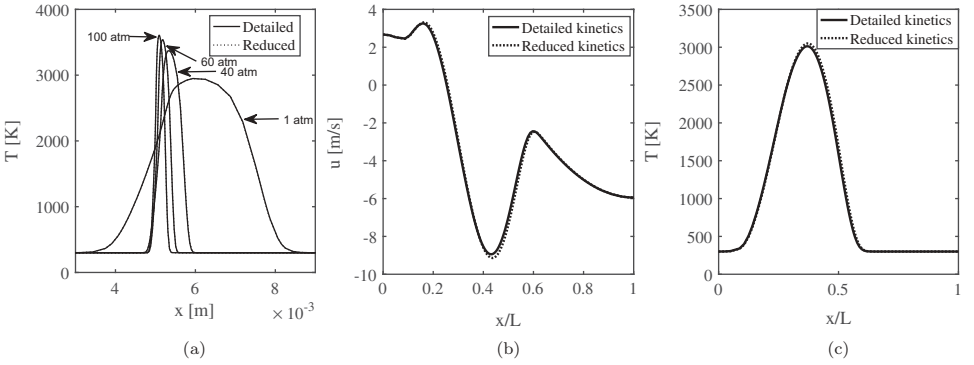

Figure 2. (a) detailed vs. reduced kinetics at $\Phi = 1$ and various pressures; (b) and (c) detailed vs. reduced kinetics at high strain rate, $p = 100$ atm, and $\Phi = 1$. (b) Velocity profile; (c) temperature profile.

et al. (2014), and Wang et al. (2015) used the so-called arc-continuation method to obtain the whole "S" curve of burning regimes. In the 1D counterflow flame, this method consists of increasing the strain rate by forcing a temperature decrease in two arbitrary internal nodes within the flame zone. There, the temperature is decreased with respect to the initial guess, which is a solution at a lower strain rate. After the iterative process converges, the new solution yields a narrower flame, the velocity at the nozzles is larger, and consequently, the strain rate increases. This method requires the replacement of the two boundary conditions for F with two internal conditions for temperature. It does not allow control over the velocity at the exit of the nozzles or the mass-flow rate ratio. Also, the velocity at the exit of the nozzles becomes very large, comparable to the speed of sound, for strain rates near the extinction limit.

For these reasons, our approach to increase the strain rate is mainly based on reducing the distance between the two nozzles. This is combined with slight increases in velocity at the exit of the nozzles to help achieve convergence. However, these velocities are kept below 10 m/s. Only the stable-burning regime is studied. Figure 3 shows our results for extinction strain rate and extinction temperature as a function of pressure. Four curves are presented. The first three are for the cases with pure methane and oxygen, and they correspond to solutions with the real-gas model with detailed kinetics, real-gas model with reduced kinetics, and ideal-gas model with detailed kinetics. The fourth curve corresponds to the case where the fuel stream is a mixture composed of methane with 40% water vapor by mass.

For the cases without inflowing water vapor, the three presented curves are compared against the data from Wang et al. (2015), where a different detailed kinetic mechanism was employed for methane and oxygen as reactants. Furthermore, the model in that publication involves the simplification that the enthalpy of the mixture equals the summation of the partial enthalpies times the mass fractions of the species. Several points are extracted from Figure 3a. Good agreement for extinction strain rate is found between the four curves at pressures up to 20 atm. Relative differences between the ideal-gas and real-gas models increase with pressure, starting at 4.5% at 20 atm and growing to 15% at 100 atm. Differences between detailed and reduced kinetics with the real-gas model are lower for all pressures, maxing at almost 8%. The extinction strain rate is linear with pressure up to 50 atm for all the detailed-kinetics models, and up to 20 atm for the reduced-kinetics model.

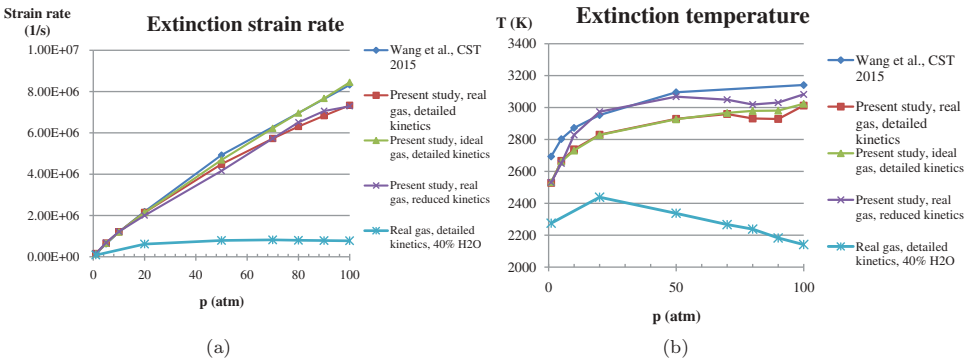

Figure 3. (a) Extinction strain rate and (b) extinction temperature as a function of pressure ($\Phi = 1$).

At higher pressure values, the gradient of extinction strain rate with respect to pressure decreases. The ideal-gas solution implies higher extinction strain rates for pressures above 20 atm compared to our real-gas results, both with detailed and reduced kinetics. This is consistent with the fact that higher flame temperatures are obtained with the ideal-gas model, as reported in Jordà Juanós and Sirignano (2017), which results in flames that are harder to extinguish. The ideal-gas result is closest with that from Wang et al. (2015).

The extinction temperature is displayed in Figure 3b. Results in the present study generally give lower temperatures than in Wang et al. (2015). The discrepancies are associated with a combination of factors, such as the use of a different reaction mechanism, as well as the simplification in calculating the mixture enthalpy. Near extinction, higher strain rates imply lower flame temperatures. Very good agreement is found between our real- and ideal-gas cases with detailed kinetics for pressures up to 70 atm. The major discrepancies appear at 80 atm and 90 atm, and there is good agreement at 100 atm. At a given strain rate, the use of reduced kinetics results in higher flame temperatures, as shown in the previous subsection. Thus, it is not surprising that the extinction flame temperature for the reduced kinetics is above the temperature corresponding to our detailed-kinetics computations for all strain rates above 5 atm. Another interesting feature is that extinction flame temperature above 50 atm was reported to increase moderately and linearly with pressure (Wang et al., 2015). However, only two data points were reported, at 50 atm and 100 atm. Several intermediate pressure values are studied herein, and a local decrease in extinction temperature is found between 70 atm and 90 atm. This occurs in all of our cases, both with detailed and reduced kinetics. The effect also appears in our ideal-gas solutions, although more modestly. It is conceivable that the model in Wang et al. (2015) would also predict a similar local decrease in extinction temperature for the mentioned pressure range, but this was not addressed.

The local minimum in extinction temperature shown in Figure 3b can be explained. At fixed composition and enthalpy for a real gas, the temperature decreases almost linearly with increasing pressure while, for an ideal gas, it remains constant. This is represented in Figure 4a, where the real-gas adiabatic flame temperature calculations are for a stoichiometric global one-step reaction of methane and oxygen becoming water vapor and carbon dioxide, and the initial temperature of the reactants is prescribed to 298.15 K. The

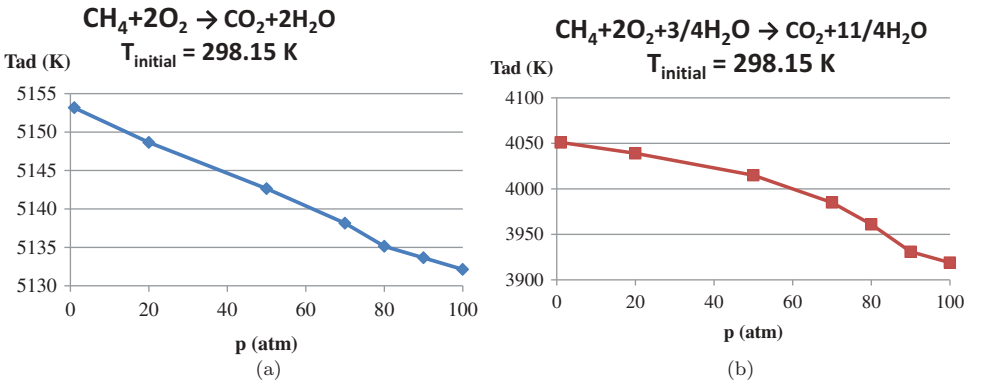

Figure 4. Adiabatic flame temperature for a real gas and complete combustion of methane and oxygen with initial temperature of 298.15 K: (a) 0% water vapor and (b) 40% water vapor.

enthalpy for an adiabatic flame without dissociation is totally determined by initial conditions and heats of formation; for the diffusion flame, these are also dominant factors. Now, in Figure 3b, composition is not fixed; rather, as shown for the ideal gas, the reduced dissociation with increasing pressure causes a superlinear variation of temperature at high pressures. The combination of the superlinear increase with the linear decrease for the real gas is the likely cause of the temperature minimum, which previous investigators did not capture.

Temperature variations at constant pressure have substantial effects on dissociation. The local minimum in extinction temperature described above has a direct effect on mass fractions of species such as hydrogen and carbon dioxide. These variables are displayed in Figure 5. CO_2 mass fraction increases from 50 atm to 70 atm, both for real and ideal gas cases with detailed kinetics. This is consistent with the increase in extinction temperature. From 70 atm to 90 atm, the mass fraction decreases, and then increases again from 90 atm to 100 atm. This inflection is also consistent with the extinction temperature trend. Similarly, for the reduced kinetics case, CO_2 mass fraction decreases from 50 atm to 90 atm, and then increases from 90 atm to 100 atm, also following the extinction temperature tendency.

All three cases show a reduction in H_2 mass fraction from 50 atm to 90 atm followed by an increase in mass fraction from 90 atm to 100 atm. Thus, this trend does not correlate as well with the extinction temperature as for CO_2.

At the extinction strain rate, the trends in compressibility factor and enthalpy departure function do not change as pressure is increased, as shown in Figure 6. Comparison is made for these two variables between the cases with detailed and reduced kinetics, resulting in good agreement.

The case where the fuel stream is a mixture with 60% methane and 40% water vapor mass fractions is now discussed. Extinction strain rate and temperature are also presented in Figure 3. Extinction strain rate occurs at a much lower magnitude for all pressures

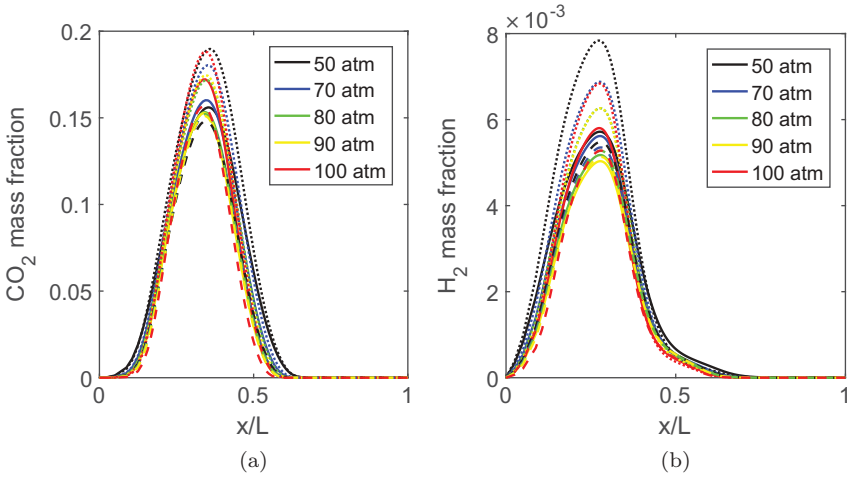

Figure 5. (a) CO_2 mass fraction and (b) H_2 mass fraction at extinction strain rate ($\Phi = 1$). Solid line is for real gas with detailed kinetics; dotted line is for real gas with reduced kinetics; dashed line is for ideal gas with detailed kinetics.

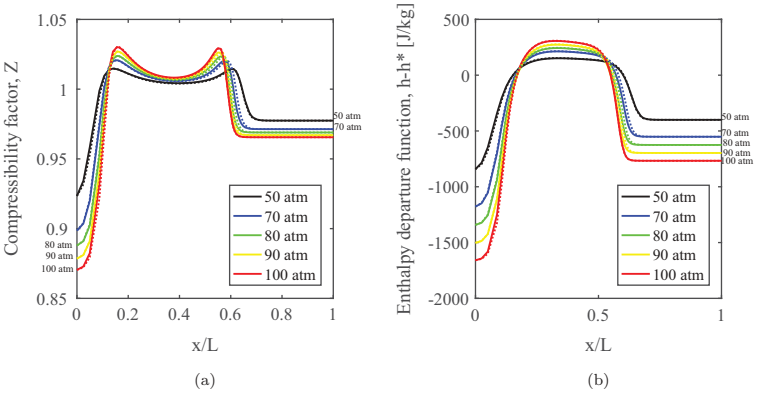

Figure 6. (a) Compressibility factor and (b) enthalpy departure function at extinction strain rate ($\Phi = 1$). Solid line is for real gas with detailed kinetics; dotted line is for real gas with reduced kinetics.

above 1 atm compared with the case with no water. In other words, it is much easier to blow off the flame given all the extra water vapor. Strain rate increases with pressure and is bounded above at 70 atm. Higher pressures decrease it by 1% to 2% for each 10 atm until 100 atm.

Extinction temperature behavior is very different from the previous case. Now, it increases between 1 atm and 20 atm and it decreases almost linearly for higher pressures up to 100 atm. The reduced dissociation with increasing pressure is a dominating factor for this initial pressure range. However, other factors play an important role for higher pressures. For example, a plot in Figure 4b of adiabatic flame temperature versus pressure for a real gas considering the presence of extra water reveals a stronger pressure effect compared to the case with no inflowing water. The difference in adiabatic flame temperature is around 20 K for the case with no water, while it is about 132 K for the case with water. This element alone does not explain the much greater drop in extinction temperature shown in Figure 3b, which is almost 300 K.

To further analyze this temperature difference, the mass-fraction values of the major species are given in Table 1 at the peak-temperature coordinate. Carbon dioxide mass fraction first increases from 1 atm to 20 atm and then decreases until 100 atm. Carbon monoxide mass fraction also decreases with pressure. The carbon reduction is explained by looking at methane mass fraction, which has the opposite behavior, first decreasing from 1 atm to 20 atm and then increasing until 100 atm. Thus, less methane is burned in the hottest flame region with increasing pressure above 20 atm, which contributes to lower flame temperatures. Note that the summation of the major species shown in Table 1 account for 97% or more of the total mass.

Table 1. Major-species mass fractions at peak-temperature coordinate and various pressures.

p (atm)	Y_{CH_4}	Y_{O_2}	Y_{H_2O}	Y_{CO_2}	Y_{CO}	Y_{H_2}	$\sum Y_{major}$	T_{max} (K)
1	0.0088	0.3699	0.3177	0.1173	0.1527	0.0032	0.9696	2275.10
20	0.0046	0.407	0.3086	0.1427	0.1163	0.0016	0.9808	2438.30
50	0.009	0.4217	0.3078	0.1259	0.1183	0.0014	0.9841	2337.10
100	0.0162	0.4552	0.293	0.1038	0.1115	0.0011	0.9808	2141.30

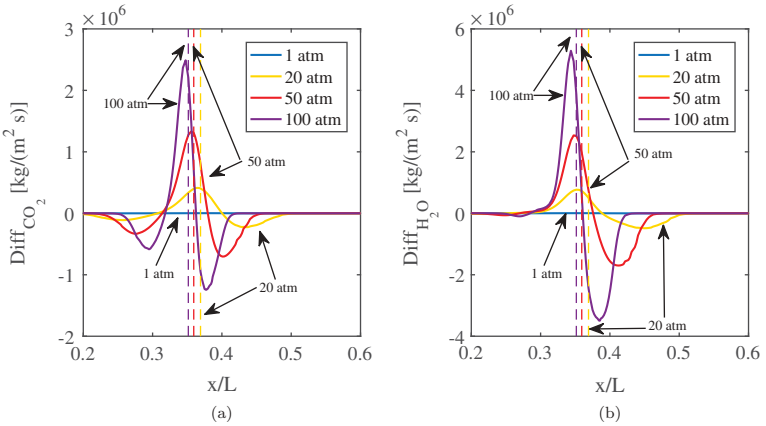

Figure 7. Diffusion fluxes in the flame region at various pressures: (a) CO_2 and (b) H_2O.

Figure 7 shows the mass-diffusion fluxes for carbon dioxide and water vapor at different pressures in the flame region. The location of the maximum flame temperature is marked with vertical dashed lines at the different pressures of interest. The ratio between the maximum diffusion fluxes of CO_2 to H_2O decrease with pressure from 0.54 at 20 atm to 0.47 at 100 atm. With the given mass fractions from Table 1, the computed ratio of mass-diffusion velocities for the same two species increase from 1.16 at 20 atm to 1.32 at 100 atm. Carbon dioxide is therefore diffusing away faster than water vapor and the difference increases with pressure, indicating that there is more water content build-up, which in turn lowers the flame temperature.

Mass-flow rate ratio

The effects on the flame position and structure are studied in this subsection when Φ has its value ranging from 0.5 to 2.5. Figure 8 shows velocity profiles and temperature profiles as a function of pressure and Φ. Increasing the oxygen-to-fuel ratio translates into a

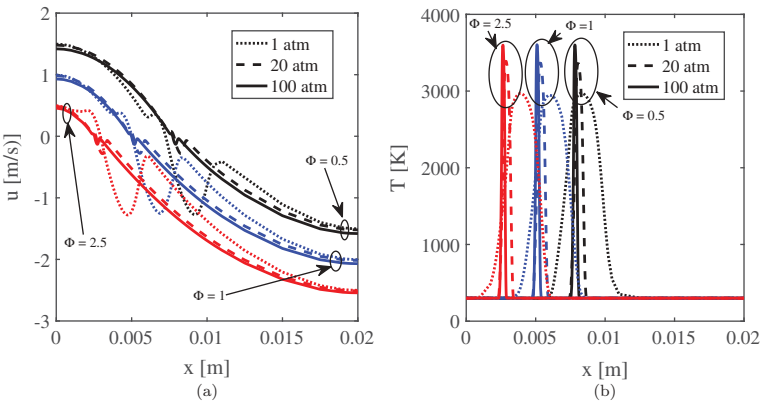

Figure 8. (a) Velocity profiles and (b) temperature profiles. Red: Φ = 2.5; Blue: Φ = 1.0; Black: Φ = 0.5.

higher oxygen mass-flow rate, and it pushes the flame towards the fuel nozzle. Contrarily, decreasing Φ displaces the flame towards the oxygen nozzle. When $\Phi = 1$, the oxygen mass-flow rate is four times greater than the methane mass-flow rate. Therefore, the flame seats closer to the fuel nozzle. Increasing pressure has the same effects on the maximum flame temperature and thickness, regardless of the value of Φ. This analysis differs from Jordà Juanós and Sirignano (2017). There, the boundary conditions were varied to match the momentum fluxes or to match mass-flow-rate fluxes between the two nozzles. Nevertheless, the consequences on the flame were the same as those demonstrated in this section for different mixture ratios.

Conclusions

This numerical study presents solutions for the 1D counterflow diffusion flame problem at high pressures using a real-gas model. Proper evaluation of the mixture enthalpy is considered together with the relaxation of ideal-gas assumptions commonly taken in the literature. Within this context, solutions with detailed chemical kinetic schemes are compared against results with reduced kinetics. It is concluded that the differences are negligible at low strain rates, regardless of the pressure. At high strain rates right before extinction occurs, the differences are more noticeable, but still slight (i.e., less than 2% in peak temperature). In particular, flame temperature becomes higher with use of reduced kinetics, which causes a greater local flow speed near the flame region. This provides the obvious advantage of much faster computations using reduced kinetics with almost no error increment.

The extinction properties are studied in terms of maximum strain rate and flame temperature that allow sustaining a flame in steady state. Strain rate is increased by reducing the distance between the two nozzles instead of increasing the inflowing velocities. The latter, previously used in the literature, implies very high flow velocities approaching the speed of sound. This fact is not compatible with the assumptions made in developing the model. Two cases are studied: one with pure methane flowing against oxygen, and the other with a mixture of methane and 40% water vapor (by mass) also impinging against oxygen.

For the case with no inflowing water, our results indicate that the flame extinguishes at lower strain rates than previously reported, especially when pressure is higher than 20 atm. Differences between the ideal-gas and real-gas models increase with pressure and are as great as 15% at 100 atm. Differences between using detailed and reduced kinetics with the real-gas model are, at most, 8%. Extinction flame temperature is also lower than in previous studies. In prior research by Wang et al. (2015), a linear and moderate increase in extinction temperature was assumed when pressure was increased between 50 atm and 100 atm because no intermediate calculations were presented. However, a local decrease in extinction temperature is obtained herein for pressures of 70 atm, 80 atm, and 90 atm. This is associated with the combination of two opposite effects of increasing pressure: one is that the real-gas adiabatic flame temperature decreases with pressure for constant enthalpy and composition, and the other is that less dissociation occurs with increasing pressure, which in turn causes higher temperature.

Extinction properties for the case with extra water vapor are substantially different. Extinction strain rate is much lower for all pressures, and even though it increases from 1 atm to 20 atm, it reaches almost an asymptotic value for higher pressures. Extinction temperature increases substantially from 1 atm to 20 atm due to the reduced dissociation. However, it decreases almost linearly with increasing pressure until 100 atm. Three factors are emphasized in relation to this trend: (i) the adiabatic flame temperature at constant enthalpy and composition decreases much faster with extra water than without it; (ii) less methane burns in the peak temperature region for pressures between 20 atm and 100 atm; and (iii) carbon dioxide diffuses faster than water vapor with increasing pressure, implying the accumulation of water, which in turn lowers the flame temperature.

Finally, the effects of varying the mass-flow rate ratio between the two nozzles are also assessed, concluding that it only produces a shift in the flame position without affecting its structure or temperature.

Acknowledgment

The first author gratefully acknowledges the Balsells Fellowship support.

Funding

This research was supported by the NSF under Grant CBET-1333605.

References

Chung, T., Ajlan, M., Lee, L.L., and Starling, K.E. 1988. Generalized multiparameter correlation for nonpolar and polar fluid transport properties. *Ind. Eng. Chem. Res.*, **27**, 671–679.

Coppola, G., Coriton, B., and Gomez, A. 2009. Highly turbulent counterflow flames: A laboratory scale benchmark for practical systems. *Combust. Flame*, **156**, 1834–1843.

Figura, L., Carbone, F., and Gomez, A. 2015. Challenges and artifacts of probing high-pressure counterflow laminar diffusion flames. *Proc. Combust. Inst.*, **35**, 1871–1878.

Giovangigli, V., Matuszewski, L., and Dupoirieux, F. 2011. Detailed modeling of planar transcritical H_2–O_2–N_2 flames. *Combust. Theor. Model.*, **15**, 141–182.

Huo, H., Wang, X., and Yang, V. 2014. A general study of counterflow diffusion flames at subcritical and supercritical conditions: Oxygen/hydrogen mixtures. *Combust. Flame*, **161**, 3040–3050.

Jordà Juanós, A., and Sirignano, W.A. 2017. Pressure effects on real-gas laminar counterflow. *Combust. Flame*, **181**, 54–70.

Kee, R.J., Miller, J.A., and Evans, G.H. 1988. A computational model of the structure and extinction of strained, opposed flow, premixed methane-air flames. *Symp. (Int.) Combust.*, **22**, 1479–1494.

Kempf, A., Forkel, H., Sadiki, A., and Janicka, J. 2000. Large-eddy simulation of a counterflow configuration with and without combustion. *Proc. Combust. Inst.*, **28**, 35–40.

Kim, I.S., and Mastorakos, E. 2006. Simulations of turbulent non-premixed counterflow flames with first-order conditional moment closure. *Flow Turbul. Combust.*, **76**, 133–162.

Law, C.K. 2006. *Combustion Physics*, Cambridge University Press, Cambridge, UK.

Lu, T., and Law, C.K. 2008. A criterion based on computational singular perturbation for the identification of quasi steady state species: A reduced mechanism for methane oxidation with no chemistry. *Combust. Flame*, **154**, 761–774.

Marble, F.E., and Broadwell, J.E. 1977. The coherent flame model for turbulent chemical reactions. Project SQUID, Technical Report TRW-9-PU.

Niemann, U., Seshadri, K., and Williams, F.A. 2014. Methane, ethane, and ethylene laminar counterflow diffusion flames at elevated pressures: Experimental and computational investigations up to 2.0 mpa. *Combust. Flame*, **161**, 138–146.

Niemann, U., Seshadri, K., and Williams, F.A. 2015. Accuracies of laminar counterflow flame experiments. *Combust. Flame*, **162**, 1540–1549.

Pettit, M.W.A., Coriton, B., Gomez, A., and Kempf, A.M. 2011. Large-eddy simulation and experiments on non-premixed highly turbulent opposed jet flows. *Proc. Combust. Inst.*, **33**, 1391–1399.

Piller, L., Idir, M., Molet, J., Matynia, A., and de Persis, S. 2015. Experimental study and modelling of nox formation in high pressure counter-flow premixed CH_4/air flames. *Fuel*, **150**, 394–407.

Prausnitz, J.M., Lichtenthaler, R.N., and de Azevedo, E.G. 1999. *Molecular Thermodynamics of Fluid-Phase Equilibria*, Prentice Hall PTR, Englewood Cliffs, N.J.

Rao, Y.V.C. 1997. *Chemical Engineering Thermodynamics*, Universities Press.

Reaction Design. 2013. Chemkin 10131, San Diego, CA.

Ribert, G., Zong, N., Yang, V., Pons, L., Darabiha, N., and Candel, S. 2008. Counterflow diffusion flames of general fluids: Oxygen/hydrogen mixtures. *Combust. Flame*, **154**, 319–330.

Ricchiuti, V., Padilla, R.E., Karnani, S., and Dunn-Rankin, D. 2013. Cantera simulations of water-laden methane/air nonpremixed counterflow flames. Presented at the 8th U.S. National Combustion. Meeting.

Smith, G.P., Golden, D.M., Frenklach, M., Moriarty, N.W., Eiteneer, B., Goldenberg, M., Bowman, C. T., Hanson, R.K., Song, S., Gardiner, Jr., W.C., Lissianski, V.V., and Qin, Z., 2000. *Gri-mech 3.0*. http://www.me.berkeley.edu/gri_mech/

Smooke, M.D., Puri, I.K., and Seshadri, K. 1986. A comparison between numerical calculations and experimental measurments of the structure of a counterflow diffusion flame burning diluted methane in diluted air. *Symp. (Int.) Combust.*, **21**, 1783–1792.

Soave, G. 1972. Equilibrium constants from a modified Redlich-Kwong equation of state. *Chem. Eng. Sci.*, **27**, 1197–1203.

Soave, G., Gamba, S., and Pellegrini, L.A. 2010. SRK equation of state: Predicting binary interaction parameters of hydrocarbons and related compounds. *Fluid Phase Equilib*, **299**, 285–293.

Sung, C.J., Liu, J.B., and Law, C.K. 1995. Structural response of counterflow diffusion flames to strain rate variations. *Combust. Flame*, **102**, 481–492.

Tirunagari, R., and Pope, S. 2017. Characterization of extinction/reignition events in turbulent premixed counterflow flames using strain-rate analysis. *Proc. Combust. Inst.* **36**, 1919–1927.

Turns, S.R. 2011. *An Introduction to Combustion: Concepts and Applications*, 3rd ed., McGraw-Hill Education, Columbus OH, USA.

Wang, X., Huo, H., and Yang, V. 2015. Counterflow diffusion flames of oxygen and n-alkane hydrocarbons (CH_4-$C_{16}H_{34}$) at subcritical and supercritical conditions. *Combust. Sci. Technol.*, **187**, 60–82.

Williams, F.A. 1985. *Combustion Theory*, 2nd ed., The Benjamin/Cummings Publishing Company, Inc., Menlo Park, CA.